

# Well Balanced Adaptive Simulation of Pollutant Transport by Shallow Water Flows: Application to the Bay of Tangier

E. M. Chaabelasri<sup>1</sup>, I. Elmahi<sup>2,\*</sup>, R. Abdellaoui<sup>2</sup>, N. Salhi<sup>1</sup>

<sup>1</sup>Laboratoire de Mécanique et Energétique, Faculté des Sciences, BP 717, 60000 Oujda, Maroc

<sup>2</sup>Equipe de Modélisation et Simulation Numérique, ENSAO, Complexe universitaire, B.P. 669, 60000 Oujda, Maroc

**Abstract** A well balanced adaptive scheme is proposed for the numerical solution of the coupled non-linear shallow water equations and depth-averaged advection-diffusion pollutant transport equation. The scheme uses the Roe approximate Riemann solver with upwind discretization for advection terms and the Vazquez scheme for source terms. It is designed to handle non-uniform bed topography on triangular unstructured meshes, while satisfying the conservation property. Dynamic mesh adaptation criteria are based on the local pollutant concentration gradients. The model is validated for steady flow over irregular bed topography, recirculation due to a sidewall expansion in a frictionless channel, and pollution advection in a flat-bottomed channel. An idealized application to the simulation of pollutant dispersion in the Bay of Tangier, Morocco is presented, which demonstrates the capability of the dynamically adaptive grid model to represent water quality scenarios in a bay of non-uniform bed topography and complicated shoreline.

**Keywords** Shallow water equations, Pollutant transport, Finite volume method, Roe solver, Dynamic mesh adaptation, Unstructured meshes

## 1. Introduction

Pollution of the Strait of Gibraltar has increased significantly in recent decades as a by-product of the growth of maritime transportation activities. Pollution is particularly hazardous to ecologically sensitive coastal regions, such as the Bay of Tangier located on the southern coast of the Strait of Gibraltar. The environment of the Bay of Tangier is subjected to human impacts from nearby urban development, industry, agriculture, fisheries, and ports (including the newly operational Tangier Mediterranean Port). These activities release toxic effluent that is causing ecological damage to the bay.

Predictions of the risk posed to the water quality of the Bay of Tangier due to pollution from different sources could play an essential part in establishing guidelines for environmental remediation and protection. In particular, numerical models of flow hydrodynamics could aid decision makers in establishing effective countermeasures in order to reduce the pollutant discharges from particular sources. The numerical model presented herein solves the bay hydrodynamics in conjunction with passive species transport, enabling

the user to estimate pollutant transport, concentration distribution, and basin residence time.

The hydrodynamic module solves the two-dimensional depth-averaged shallow water equations and hence is used to investigate the forcing mechanism responsible for circulation patterns in the Bay of Tangier. Pollutant transport is modelled by means of an advection-diffusion equation for the depth-averaged concentration of substances contaminating the seawater. Herein, the resulting system of equations is formulated so that it constitutes a hyperbolic system of non-linear conservation laws with source terms.

In recent years, there has been increasing interest in the design of numerical schemes based on non-linear conservation laws. A particular challenge is to obtain high-order accurate solutions in space and time for flows over complicated bed topography. Various finite volume schemes developed for general systems of hyperbolic conservation laws have been applied to the non-linear shallow-water equations (NLSWEs), utilising upwind methods based on approximate Riemann solvers. Such solvers include Roe's method[1], monotonic upstream schemes for conservation laws (MUSCL) in curvilinear coordinate systems[2][3], essentially non-oscillatory (ENO) schemes[5][6], the weighted essentially non-oscillatory method[6], and the Harten, Lax and van Leer (HLL) solver [7]. Most of these methods are capable of capturing shock-like behaviour to a high degree of accuracy and

\* Corresponding author:  
imelmahi@gmail.com (I. Elmahi)

Published online at <http://journal.sapub.org/ijhe>

Copyright © 2014 Scientific & Academic Publishing. All Rights Reserved

perform particularly well for steep-fronted flows like discontinuous, transcritical flows over flat bed topography. However, for spatially varying bed topography, special treatment is required in order to discretise the component of the source term stemming from the bed gradient so that it properly balances the relevant flux gradient term and ensures that water at rest remains so. In a well-balanced solver, the discrete source terms balance the discrete flux terms. For example, Bermudez and Vazquez[8] proposed an upwind method for the non-linear shallow water equations with bed slope source terms, which was applied by Vazquez-Cendon[9] to a range of shallow water flow problems. LeVeque[4] proposed a Riemann solver that balanced the source terms and flux gradients in each cell of a regular computational mesh. However, the extension of this scheme for unstructured meshes is not trivial. Hubbard and Garcia-Navarro[3] proposed a further numerical treatment, in which the upwind method of Bermudez and Vazquez is used for source terms. Numerical methods based on surface gradient techniques have also been applied to shallow water equations by Zhou et al.[24].

The present paper describes a high-resolution finite volume shock-capturing scheme for the solution of the non-homogenous hyperbolic system of equations that represent shallow flow pollutant transport processes. The computational mesh is unstructured, triangular, and dynamically adaptive. The Roe's approximate Riemann solver is used for advective fluxes. Time integration is performed by means of a Runge-Kutta algorithm. The method is of high resolution and aimed at representing 2DH domains with complicated boundary and bed geometry, such as the Bay of Tangier.

The paper is organized as follows. Section 2 briefly outlines the governing equations. Section 3 deals with the construction of an efficient well-balanced high-order finite volume scheme on unstructured meshes. Section 4 describes a dynamical adaptive procedure based on multi-level refinements and unrefinements by monitoring the pollutant concentration in the computational domain. Section 5 provides details of the model validation. Section 6 presents the demonstration study of hypothetical pollutant dispersion in the Bay of Tangier. Conclusions are summarised in Section 7.

## 2. Governing Equations

In conservation form, the two-dimensional non-linear shallow water equations are given by Equations (1) to (3) below[25-26]. The depth-averaged continuity equation is

$$\frac{\partial h}{\partial t} + \frac{\partial(hu)}{\partial x} + \frac{\partial(hv)}{\partial y} = 0 \quad (1)$$

The depth-averaged momentum equations in the  $x$ - and  $y$ -directions are

$$\frac{\partial(hu)}{\partial t} + \frac{\partial(hu^2 + \frac{gh^2}{2})}{\partial x} + \frac{\partial(huv)}{\partial y} = -gh \frac{\partial Z_b}{\partial x} - ghS_{fx} \quad (2)$$

and

$$\frac{\partial(hv)}{\partial t} + \frac{\partial(huv)}{\partial x} + \frac{\partial(hv^2 + \frac{gh^2}{2})}{\partial y} = -gh \frac{\partial Z_b}{\partial y} - ghS_{fy} \quad (3)$$

where  $h$  is the total depth from the sea bed to the free surface,  $u$  and  $v$  are the depth-averaged velocity components in the Cartesian  $x$  and  $y$  directions,  $Z_b$  is the bed elevation above a fixed horizontal datum,  $g$  the acceleration due to gravity, and  $S_{fx}$  and  $S_{fy}$  are the bed shear stress components, defined as

$$S_{fx} = n_M u \frac{\sqrt{u^2 + v^2}}{h^{\frac{4}{3}}}, \quad S_{fy} = n_M v \frac{\sqrt{u^2 + v^2}}{h^{\frac{4}{3}}} \quad (4)$$

where  $n_M$  is the Manning's coefficient. Assuming the water pollutant mixture is fully mixed in the vertical direction, the depth-averaged pollution dispersion equation may be written in advection-diffusion form for a passive contaminant as,

$$\frac{\partial(hC)}{\partial t} + \frac{\partial(huC)}{\partial x} + \frac{\partial(hvC)}{\partial y} = \frac{\partial}{\partial x} (D_x h \frac{\partial C}{\partial x}) + \frac{\partial}{\partial y} (D_y h \frac{\partial C}{\partial y}) \quad (5)$$

where  $C$  is pollutant concentration, and  $D_x$  and  $D_y$  are pollutant diffusion coefficients in the  $x$  and  $y$  directions. Using matrix-vector notation, the coupled pollutant transport system can be written

$$\mathbf{W}_t + \mathbf{F}_1(\mathbf{W})_x + \mathbf{F}_2(\mathbf{W})_y - \tilde{\mathbf{F}}_1(\mathbf{W})_x - \tilde{\mathbf{F}}_2(\mathbf{W})_y = \mathbf{S}(\mathbf{W}) + \mathbf{S}_f(\mathbf{W}) \quad (6)$$

where  $\mathbf{W}$  is the vector of dependent variables,  $\mathbf{F}_1$ ,  $\mathbf{F}_2$  are the inviscid flux vectors,  $\tilde{\mathbf{F}}_1$ ,  $\tilde{\mathbf{F}}_2$  the diffusive flux vectors,  $\mathbf{S}$  is the vector of source terms describing the bed variations,  $\mathbf{S}_f$  describes the friction terms, and the subscripts  $x$ ,  $y$ , and  $t$  denote partial differentiation. In full, the vectors are

$$\mathbf{W} = \begin{pmatrix} h \\ hu \\ hv \\ hC \end{pmatrix}, \quad \mathbf{F}_1 = \begin{pmatrix} hu \\ hu^2 + \frac{gh^2}{2} \\ huv \\ huC \end{pmatrix}, \quad \mathbf{F}_2 = \begin{pmatrix} hv \\ huv \\ hv^2 + \frac{gh^2}{2} \\ hvC \end{pmatrix},$$

$$\tilde{\mathbf{F}}_1 = \begin{pmatrix} 0 \\ 0 \\ 0 \\ \frac{\partial}{\partial x} (hD_x \frac{\partial C}{\partial x}) \end{pmatrix}, \quad \tilde{\mathbf{F}}_2 = \begin{pmatrix} 0 \\ 0 \\ 0 \\ \frac{\partial}{\partial y} (hD_y \frac{\partial C}{\partial y}) \end{pmatrix}, \quad (7)$$

and

$$\mathbf{S} = \begin{pmatrix} 0 \\ -gh \frac{\partial Z_b}{\partial x} \\ -gh \frac{\partial Z_b}{\partial y} \\ 0 \end{pmatrix}, \quad \mathbf{S}_f = \begin{pmatrix} 0 \\ -gh S_{fx} \\ -gh S_{fy} \\ 0 \end{pmatrix}$$

### 3. Numerical Model

The flow domain is partitioned into a set of triangular cells or finite volumes,  $V_i \subset \mathbb{R}^2$ . Let  $\Gamma_{ij}$  be the common edge of two neighbouring cells  $V_i$  and  $V_j$ , with  $|\Gamma_{ij}|$  its length,  $N(i)$  is the set of neighbouring triangles of cell  $V_i$ , and  $\vec{\mathbf{n}}_{ij} = (n_x, n_y)$  is the unit vector normal to the edge  $\Gamma_{ij}$  and points toward the cell  $V_j$  (see Fig. 1). A cell-centred finite volume method is then formulated where

all dependent variables are represented as piecewise constant in the cell as follows,

$$\mathbf{W}_i = \frac{1}{|V_i|} \int_{V_i} \mathbf{W} dV$$

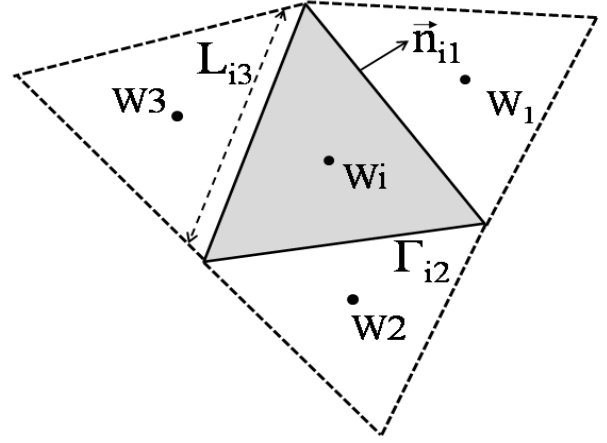


Figure 1. Cell-centred control volume

For the triangular elements used here, the integral around the element is written as the sum of the contributions from each edge, such that

$$\begin{aligned} & \frac{(\mathbf{W}_i^{n+1} - \mathbf{W}_i^n)}{\Delta t} |V_i| + \sum_{j \in N(i)} \int_{\Gamma_{ij}} \mathbf{F}(\mathbf{W}^n, \vec{\mathbf{n}}) d\Gamma - \sum_{j \in N(i)} \int_{\Gamma_{ij}} \tilde{\mathbf{F}}(\mathbf{W}^n, \vec{\mathbf{n}}) d\Gamma \\ &= \int_{V_i} \mathbf{S}(\mathbf{W}^n) dV + \int_{V_i} \mathbf{S}_f(\mathbf{W}^n) dV \end{aligned} \quad (8)$$

where  $\mathbf{W}_i^n = \mathbf{W}(x_i, x_i, t_n)$  is the vector of conserved variables evaluated at time level  $t_n = n\Delta t$ ,  $n$  is the number of time steps,  $\Delta t$  is the time step, and  $|V_i|$  is the area of cell  $V_i$ . To evaluate the state  $\mathbf{W}_i^n$ , an approximation is required of the convective and diffusive flux terms at each edge of the cell. The integral along the  $i$ - $j$  edge of a control volume of the normal flux  $\mathbf{F}(\mathbf{W}^n, \vec{\mathbf{n}}) = \mathbf{F}_1 n_x + \mathbf{F}_2 n_y$  can be written,

$$\int_{\Gamma_{ij}} \mathbf{F}(\mathbf{W}^n, \vec{\mathbf{n}}) d\Gamma = \Phi(\mathbf{W}_i^n, \mathbf{W}_j^n, \vec{\mathbf{n}}_{ij}) \cdot \mathbf{L}_{ij} \quad (9)$$

where  $\Phi$  is the numerical flux vector and  $\mathbf{L}_{ij}$  is the edge length of  $\Gamma_{ij}$ . Herein, the following upwind scheme based on Roe's approximate Riemann solver is employed to determine  $\Phi$  on the control volume surfaces. At each cell edge[10],

$$\Phi(\mathbf{W}_i, \mathbf{W}_j, \vec{\mathbf{n}}_{ij}) = \frac{1}{2} \left( \mathbf{F}(\mathbf{W}_i, \vec{\mathbf{n}}_{ij}) + \mathbf{F}(\mathbf{W}_j, \vec{\mathbf{n}}_{ij}) \right) - \frac{1}{2} \left| \mathbf{A}(\tilde{\mathbf{W}}, \vec{\mathbf{n}}_{ij}) \right| (\mathbf{W}_j - \mathbf{W}_i) \quad (10)$$

in which

$$\left| \mathbf{A}(\tilde{\mathbf{W}}, \vec{\mathbf{n}}_{ij}) \right| = \mathbf{R}(\tilde{\mathbf{W}}, \vec{\mathbf{n}}_{ij}) \left| \mathbf{A}(\tilde{\mathbf{W}}, \vec{\mathbf{n}}_{ij}) \right| \mathbf{L}(\tilde{\mathbf{W}}, \vec{\mathbf{n}}_{ij}) \quad (11)$$

where  $\mathbf{A}(\tilde{\mathbf{W}}, \vec{\mathbf{n}}_{ij})$  is the flux Jacobian evaluated using Roe's average state,  $\mathbf{R}$  and  $\mathbf{L}$  are the right and left eigenvector matrices of  $\mathbf{A}$ , and  $|\mathbf{A}|$  is a diagonal matrix of the absolute values of the eigenvector of  $\mathbf{A}$ . For the system given by Equation (6), the flux Jacobian is given by,

$$\mathbf{A}(\tilde{\mathbf{W}}, \hat{\mathbf{n}}_{ij}) = \begin{pmatrix} 0 & n_x & n_y & 0 \\ (g\tilde{h} - \tilde{u}^2)n_x - \tilde{u}\tilde{v}n_y & 2\tilde{u}n_x + \tilde{v}n_y & \tilde{u}n_y & 0 \\ -\tilde{u}\tilde{v}n_x + (g\tilde{h} - \tilde{v}^2)n_y & \tilde{v}n_x & \tilde{u}n_x + 2\tilde{v}n_y & 0 \\ -\tilde{C}(\tilde{u}n_x + \tilde{v}n_y) & \tilde{C}n_x & \tilde{C}n_y & \tilde{C}(\tilde{u}n_x + \tilde{v}n_y) \end{pmatrix} \quad (12)$$

which has real eigenvalues given by

$$\begin{cases} \lambda_1 = \tilde{u}n_x + \tilde{v}n_y - \tilde{C} \\ \lambda_2 = \lambda_3 = \tilde{u}n_x + \tilde{v}n_y \\ \lambda_4 = \tilde{u}n_x + \tilde{v}n_y + \tilde{C} \end{cases} \quad (13)$$

$\tilde{C}$  here is the wave celerity, and  $\tilde{u}$ ,  $\tilde{v}$ ,  $\tilde{h}$  and  $\tilde{C}$  are the Roe average values defined as [10],[11]:

$$\begin{cases} \tilde{h} = \frac{h_i + h_j}{2} \\ \tilde{u} = \frac{u_i\sqrt{h_i} + u_j\sqrt{h_j}}{\sqrt{h_i} + \sqrt{h_j}} \\ \tilde{v} = \frac{v_i\sqrt{h_i} + v_j\sqrt{h_j}}{\sqrt{h_i} + \sqrt{h_j}} \\ \tilde{C} = \frac{C_i + C_j}{2} \end{cases} \quad (14)$$

A four point finite volume interpolation is used to evaluate the diffusion flux through an inner edge  $\Gamma_{ij}$ , so one has

$$\int_{\Gamma_{ij}} \nabla C \cdot \hat{\mathbf{n}} d\Gamma = \int_{\Gamma_{ij}} \frac{\partial C}{\partial n} d\Gamma = |\Gamma_{ij}| \frac{C_j - C_i}{d_{ij}}$$

where  $d_{ij} = d(x_i, \Gamma_{ij}) + d(x_j, \Gamma_{ij})$ , and  $x_i$  is the intersection of the orthogonal bisectors of the edges of the triangle  $V_i$  and  $d(x_i, \Gamma_{ij})$  is the distance between  $x_i$  and the edge  $\Gamma_{ij}$ .

The slope variation's source terms are balanced by means of a two-dimensional implementation of the upwind scheme proposed by Vazquez et al.[9][12] for treating the non homogeneous part of Saint-Venant equations, and which satisfies the exact conservation C-property. Integration of the source term on the control volume  $V_i$  is written,

$$\int_{V_i} \mathbf{S}^n(\mathbf{W}) dV = \sum_{j \in N(i)} \int_{\Gamma_{ij}} \mathbf{S}^n(\mathbf{W}, \hat{\mathbf{n}}_{ij}) d\Gamma \quad (15)$$

Following Bermudez[13], this approximation is upwinded and the source term  $\mathbf{S}^n$  replaced by a numerical source vector  $\boldsymbol{\Psi}^n$ , such that

$$\int_{\Gamma_{ij}} \mathbf{S}^n(\mathbf{W}, \hat{\mathbf{n}}_{ij}) d\Gamma = \boldsymbol{\Psi}^n(\mathbf{X}_i, \mathbf{X}_j, \mathbf{W}_i, \mathbf{W}_j, \hat{\mathbf{n}}_{ij}) |\Gamma_{ij}| \quad (16)$$

At each cell interface  $\Gamma_{ij}$ , the contribution of the source term at the point  $\mathbf{X}_{ij}$  is defined as the projection of the source term vector in the basis of eigenvectors of the Jacobian matrix. Thus the source term function is,

$$\begin{aligned} \boldsymbol{\Psi}^n(\mathbf{X}_i, \mathbf{X}_j, \mathbf{W}_i, \mathbf{W}_j, \hat{\mathbf{n}}_{ij}) \\ = [\mathbf{I} - \mathbf{A}(\tilde{\mathbf{W}}, \hat{\mathbf{n}}_{ij}) \mathbf{A}(\tilde{\mathbf{W}}, \hat{\mathbf{n}}_{ij})] \cdot \hat{\mathbf{S}}^n(\mathbf{X}_i, \mathbf{X}_j, \mathbf{W}_i, \mathbf{W}_j, \hat{\mathbf{n}}_{ij}) \end{aligned} \quad (17)$$

where  $\mathbf{I}$  is the identity matrix, and  $\hat{\mathbf{S}}^n(\mathbf{X}_i, \mathbf{X}_j, \mathbf{W}_i, \mathbf{W}_j, \hat{\mathbf{n}}_{ij})$  represents an approximation of the source term on the cell interface  $\Gamma_{ij}$ . Its choice is crucial to obtain accurate results. Using states  $\mathbf{W}_i$  and  $\mathbf{W}_j$ , the approximation  $\hat{\mathbf{S}}^n$  is defined by [13] as

$$\hat{\mathbf{S}}^n(\mathbf{X}_i, \mathbf{X}_j, \mathbf{W}_i, \mathbf{W}_j, \hat{\mathbf{n}}_{ij}) = \begin{bmatrix} 0 \\ g\sqrt{h_i h_j} \frac{(Zb_i - Zb_j)}{d_{ij}} n_x \\ g\sqrt{h_i h_j} \frac{(Zb_i - Zb_j)}{d_{ij}} n_y \\ 0 \end{bmatrix} \quad (18)$$

To obtain higher-order spatial accuracy, the fluxes at each edge are calculated using a piecewise linear function of the state variable  $\mathbf{W}$  inside the control volume. For the cell-centred mesh, the MUSCL (Monotonic Upstream Centred Scheme for Conserved Laws) approach is adopted, whereby the left and right values of the states variable are evaluated from

$$\begin{cases} \mathbf{W}_{ij}^L = \mathbf{W}_i + \frac{1}{2} \nabla \mathbf{W}_i \cdot \mathbf{N}_{ij} \\ \mathbf{W}_{ij}^R = \mathbf{W}_j - \frac{1}{2} \nabla \mathbf{W}_j \cdot \mathbf{N}_{ij} \end{cases} \quad (19)$$

in which  $\mathbf{N}_{ij}$  is the vector distance between the barycentre coordinates of cells  $V_i$  and  $V_j$ . The gradient components  $\frac{\partial \mathbf{W}_i}{\partial x}$   $\frac{\partial \mathbf{W}_j}{\partial x}$  of the state variables are calculated by minimizing the quadratic function[11]:

$$\theta_i(X, Y) = \sum_{j \in N(i)} \left| \mathbf{W}_i + (x_j - x_i)X + (y_j - y_i)Y - \mathbf{W}_j \right|^2$$

The MUSCL approach gives a second-order spatial approximation. However, numerical oscillations can occur when evaluating the normal gradients of the state variables, and so a slope limiter is usually applied. Here we consider two candidate limiters: (1) the Van Albada limiter,

$$g(x, y) = \begin{cases} 0 & \text{if } xy < 0 \\ \frac{(x^2 + \varepsilon)y + (y^2 + \varepsilon)x}{x^2 + y^2 + 2\varepsilon} & \text{elsewhere} \end{cases} \quad (20)$$

where  $0 < \varepsilon \leq 1$  ; and (2) the Minmod limiter, with general form,

$$\frac{\partial^{\text{lim}} \mathbf{W}_i}{\partial x} = \frac{1}{2} \left[ \min_{j \in V'(i)} \text{sgn}\left(\frac{\partial \mathbf{W}_j}{\partial x}\right) + \max_{j \in V'(i)} \text{sgn}\left(\frac{\partial \mathbf{W}_j}{\partial x}\right) \right] \min_{j \in V'(i)} \left| \frac{\partial \mathbf{W}_j}{\partial x} \right| \quad (21a)$$

and

$$\frac{\partial^{\text{lim}} \mathbf{W}_i}{\partial y} = \frac{1}{2} \left[ \min_{j \in V'(i)} \text{sgn}\left(\frac{\partial \mathbf{W}_j}{\partial y}\right) + \max_{j \in V'(i)} \text{sgn}\left(\frac{\partial \mathbf{W}_j}{\partial y}\right) \right] \min_{j \in V'(i)} \left| \frac{\partial \mathbf{W}_j}{\partial y} \right| \quad (21b)$$

For the purpose of time integration, Equation (6) is expressed as

$$\frac{\partial \mathbf{W}}{\partial t} = \phi(\mathbf{W}) \quad (22)$$

where  $\phi$  is an operator that includes the transport, diffusion and source terms of the system.

For explicit time integration, TVD Runge–Kutta methods[14] or other ODE solvers can be applied to (22) to achieve a suitable order of accuracy in time. For the present work the second-order Runge–Kutta method has been adopted, given by,

$$\mathbf{W}^{n+1} = \mathbf{W}^n + \frac{\Delta t}{2} \phi(\bar{\mathbf{W}}) \quad (23)$$

in which

$$\bar{\mathbf{W}} = \mathbf{W}^n + \Delta t \phi(\mathbf{W}^n)$$

To ensure stability of the present explicit scheme, the time step is set according to the Courant-Friedrichs-Lewy (CFL) criterion[14], giving:

$$\Delta t = CFL \min_{ij} \left( \frac{|V_i| + |V_j|}{2|\Gamma_{ij}| \max(|(\lambda_p)_{ij}|)} \right) \quad (24)$$

where  $CFL$  is the Courant number ( $0 < CFL \leq 1$ ).

The boundary conditions are as follows: At a slip wall boundary, the velocity is projected tangentially onto the wall and there is no flux through the solid boundary. At a non-slip wall boundary,  $u_n = 0$  and  $v_n = 0$ . Open boundary conditions are set by the outgoing Riemann invariants for sub-critical inflow and outflow.

## 4. Dynamically Adaptive Triangular Mesh

The mesh generation is based on the Delaunay triangulation[28], which uses a curvature-dependent generation strategy designed to produce smaller elements in regions of high curvature in the spatial domain. To improve computational performance, an optimal mesh is used in regions of high gradient in the physical variables (e.g. at a flow discontinuity). An

adaptive procedure based on multilevel coarsening and refinement is implemented, aimed at constructing an adaptive mesh that dynamically follows the unsteady solution of the physical problem. Initially, a coarse mesh covers the computational domain. From then on, using the solution as it evolves, we establish a criterion function that identifies volumes that should be refined. The adaption criterion is based on the normalized concentration of the pollutant or water level,

$$\text{Crit}(\tau_i) = \frac{C(\tau_i)}{\max_{K \in \Omega_h} C(K)} / \frac{h(\tau_i)}{\max_{K \in \Omega_h} h(K)} \quad (25)$$

where  $\Omega_h$  is the triangulation of the domain,  $C(\tau_i)$  and  $h(\tau_i)$  are the pollutant concentration and the water depth at cell  $\tau_i$ . A list (L) is then established of triangles that must either be refined or coarsened based on the value of the adaptation criterion. An array of integers is used to define, for each triangle of the coarse mesh, the level,  $m$ , of required adaptation. For example, during refinement a hierarchical multi-level of triangles is created (see Figure 2). For more details about the algorithm, we refer the reader to references[15][16][17].

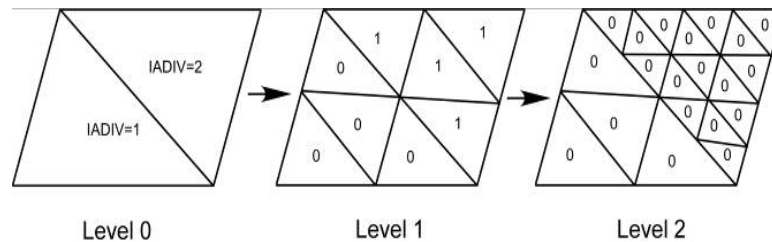


Figure 2. Example of two levels of triangular mesh refinement

## 5. Model Validation

The numerical scheme has been validated against several benchmark tests, including 1D steady open channel flow over irregular bed topography, recirculation promoted by a side wall expansion in a frictionless canal, and pollutant advection in a flat-bottomed channel. Details on these test cases can be found also in[18]. In all cases,  $g = 9.81 \text{ m/s}^2$ .

### 5.1. Validation Test 1: Steady Flow over Irregular Bed Topography

Table 1. Validation Test 1: bed elevation  $Z_b$  at point  $x$  for Goutal's case of steady flow over an irregular bed (unit: m)

$x$	0	50	100	150	250	300	350
$Z_b$	0	0	2.5	5	5	3	5
$x$	400	425	435	450	475	500	505
$Z_b$	5	7.5	8	9	9	9.1	9
$x$	530	550	565	575	600	650	700
$Z_b$	9	6	5.5	5.5	5	4	3
$x$	750	800	820	900	950	1000	1500
$Z_b$	3	2.3	2	1.2	0.4	0	0

For finite volume solvers of the non-linear shallow water equations that do not balance the flux gradient and source terms, spurious results are obtained in cases involving non-uniform bed topography. To validate the present numerical model for a severe case of spatially varying bed terrain, the model is applied to the benchmark problem devised by Goutal[19] of steady flow over the bed topography listed in Table 1 and illustrated in Figure 3. The bed slope is discontinuous, so this test problem provides an excellent indication as to how well a solver copes with the bed source term discretisation, and is particularly useful for testing schemes before practical application to natural watercourses. The same test case has also been used by

Vazquez-Cendon[9] and Tseng[21], among others.

The rectangular channel is 1500 m long and 40 m wide. The triangular mesh generated herein consists of 1619 elements and 1000 nodes. The initial conditions are that the free surface elevation is prescribed to be 15 m above the  $Z_b = 0 \text{ m}$  datum level, and the discharge per unit breadth is  $q = 0.75 \text{ m}^2/\text{s}$  throughout the channel. For all time  $t > 0$ , the boundary conditions are  $q = 0.75 \text{ m}^2/\text{s}$  at the upstream open boundary and  $h = 15 \text{ m}$  at the downstream open boundary. Bottom friction is neglected so that the test focused on checking the treatment of the source terms related to bed slopes.

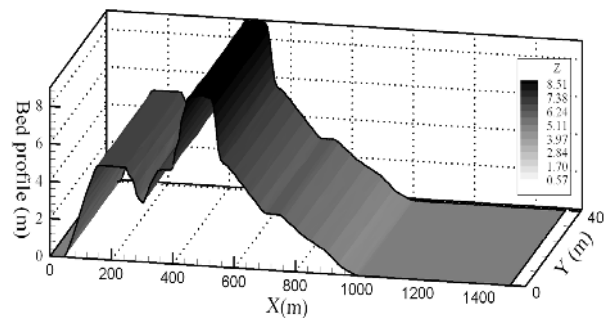
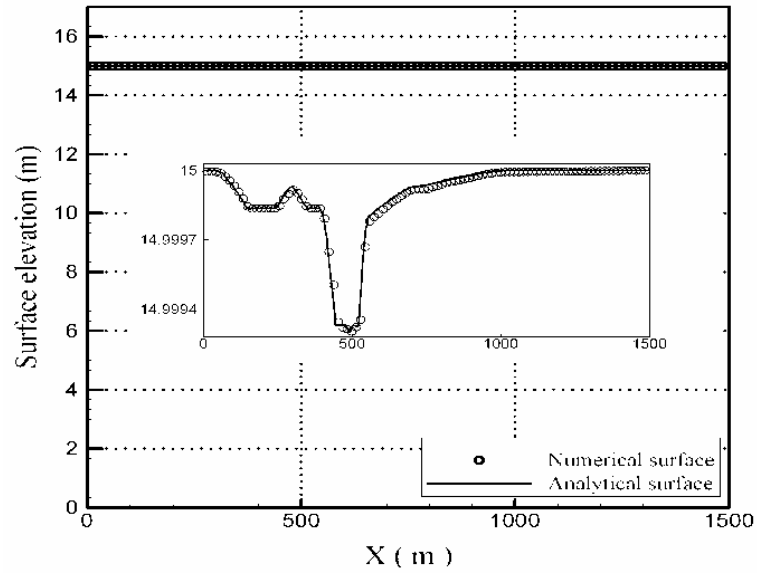
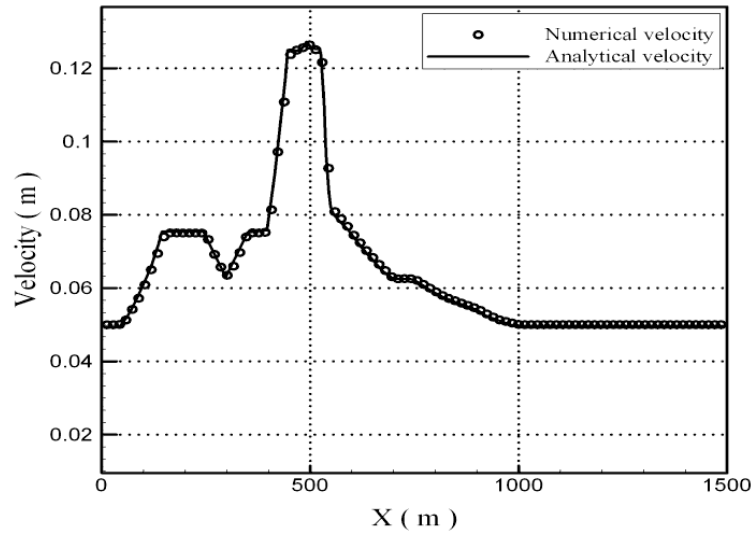


Figure 3. Validation Test 1: Bed topography of Goutal's[19] channel

Figures 4, 5 and 6 present the numerically predicted and analytical[19] free surface elevation, velocity and discharge profiles along the channel. These results were obtained by choosing a  $\text{CFL} = 0.85$ . An inset showing a close-up view is included in each figure. In general, satisfactory agreement is achieved between the numerical predictions and analytical solutions. Moreover, a qualitative comparison with the results of Le Dissez et al.[20], who used an implicit finite volume method, indicates that the relative errors in the present model are very low.



**Figure 4.** Validation Test 1: Comparison of numerical free surface elevation profile with corresponding analytical solution at steady state



**Figure 5.** Validation Test 1: Comparison of numerical velocity profile with corresponding analytical solution at steady state

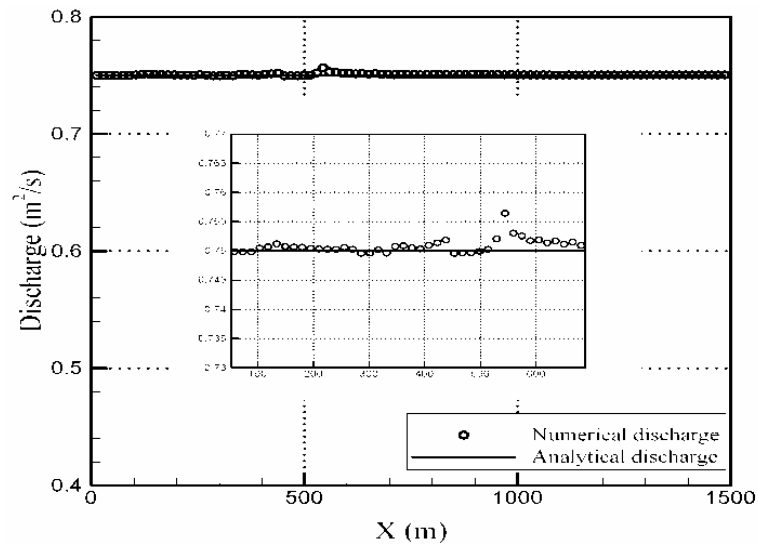


**Figure 6.** Validation Test 1: Comparison of numerical discharge profile with corresponding analytical solution at steady state

## 5.2. Validation Test 2: Recirculation due to Sidewall Expansion in Frictionless Channel

Two-dimensional laminar flow past a sudden expansion in a sidewall is next considered, in order to test the ability of the numerical model to reproduce the recirculation zone that develops behind a step due to flow separation at a step. The results will be compared against data obtained by Denham and Patrick[27] who carried out an experimental and numerical study of recirculation in a water channel containing a sidewall expansion. The channel width was 2 m before and 3 m after the expansion. The dimension of the sidewall expansion was therefore,  $b = 1$  m. The mean inflow velocity is  $U_1 = 0.5$  m/s, the flow depth at the downstream outlet is 1 m, and the eddy viscosity  $\nu = 0.00685$  m<sup>2</sup>/s corresponding to a step Reynolds number  $Re = bU_1/\nu = 72$ . The bottom friction is set to zero, and a no-slip boundary condition is imposed on the side walls. The numerical experiments are performed on a quasi-structured triangular mesh of 2048 cells with 1105 nodes (see figure 7).

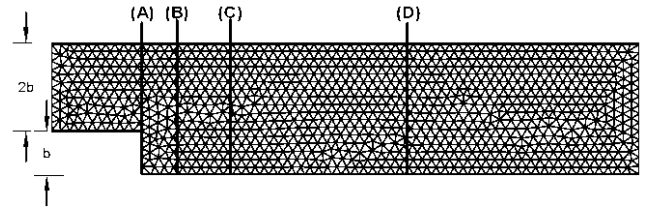


Figure 7. Validation Test 2: Triangular mesh for side-wall expansion channel

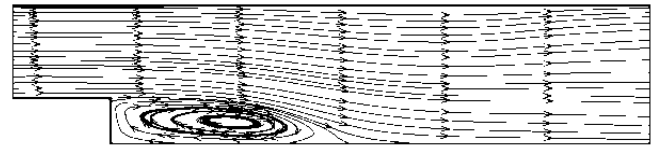


Figure 8. Validation Test 2: Stream lines and recirculation region downstream of side-wall expansion

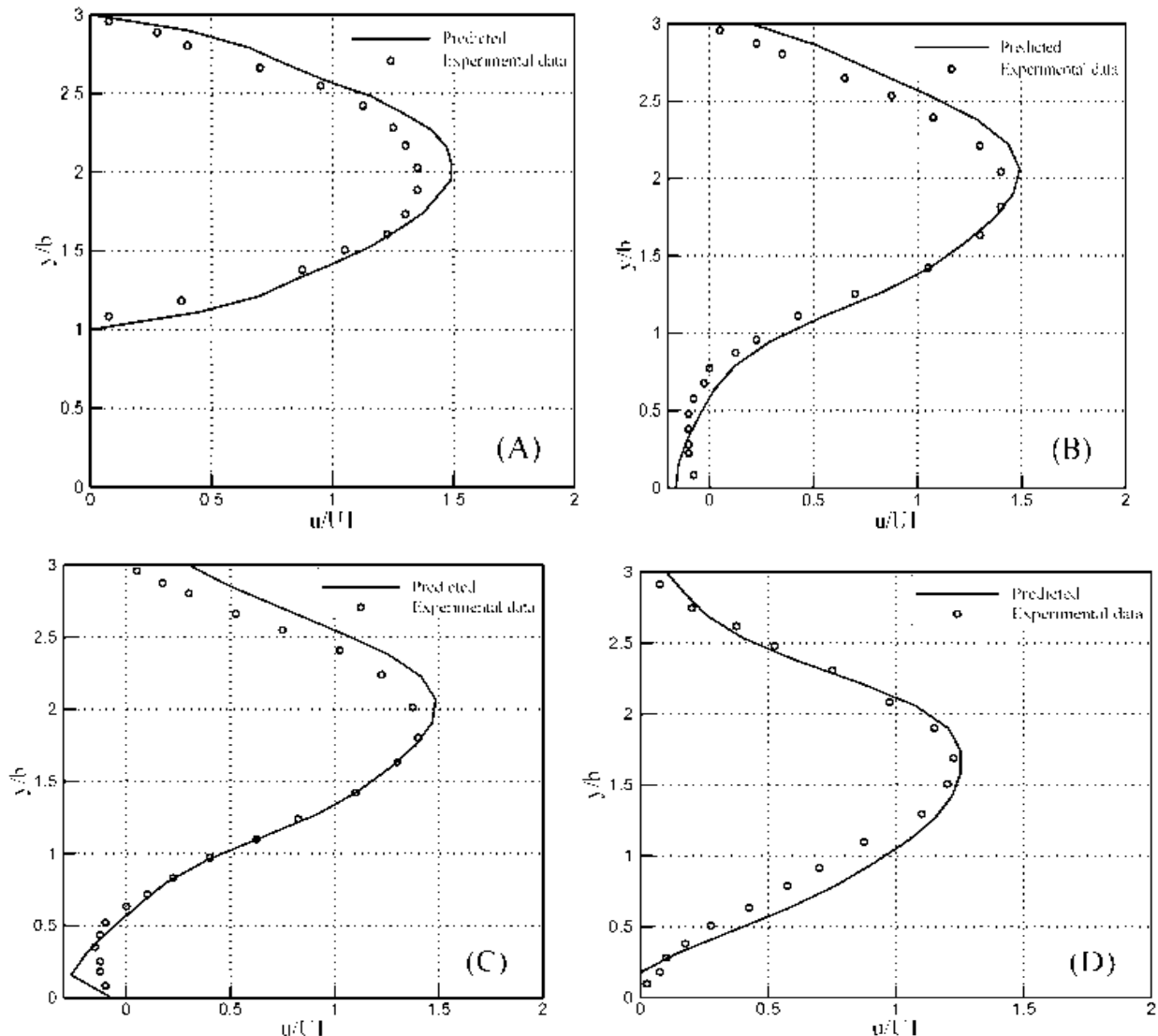


Figure 9. Validation Test 2: Transverse profiles of streamwise depth-averaged velocity component at different sections along the channel containing a side-wall expansion: (a)  $x/b = 2$ , (b)  $x/b = 2.8$ , (c)  $x/b = 4$ , and (d)  $x/b = 8$



Figure 9 presents transverse profiles of streamwise depth-averaged velocity component at different sections along the channel containing a side-wall expansion. The predicted steady-state velocity profiles at intervals along the channel past the expansion are in very close agreement with Denham and Patrick's experimental results, as can be seen in Figure 8. This recirculation zone is correctly modeled. We note, that to generate the recirculation zones, we need to do an iterative calculation finer to ensure stability and this through a variety of CFL = 0.6.

### 5.3. Validation Test 3: Pollutant Advection in a Flat-bottomed Channel

For a coarse mesh, the Roe approximate scheme can be numerically dissipative, and this can have a serious negative impact on the accurate prediction of fronts when the simulation time is long. This test examines how well the present adaptive scheme manages to reproduce pure convection of a pollutant by considering the choice of limiter and mesh adaptation criterion.

The initial conditions throughout the channel are as follows: water depth  $h_0(x, 0) = 1\text{ m}$ , depth-averaged velocity  $u_0(x, 0) = 0.05\text{ m/s}$ , and discharge per unit breadth  $q_0 = 0.05\text{ m}^2/\text{s}$ . The channel is frictionless, with a flat horizontal bed. Figure 10 shows the initial pollution concentration profile, given by a Gaussian pulse centred at  $x_1 = 0.25\text{ m}$ .

$$C(x, 0) = C_1 \exp\left(-\frac{(x - x_1)^2}{a}\right) \quad (26)$$

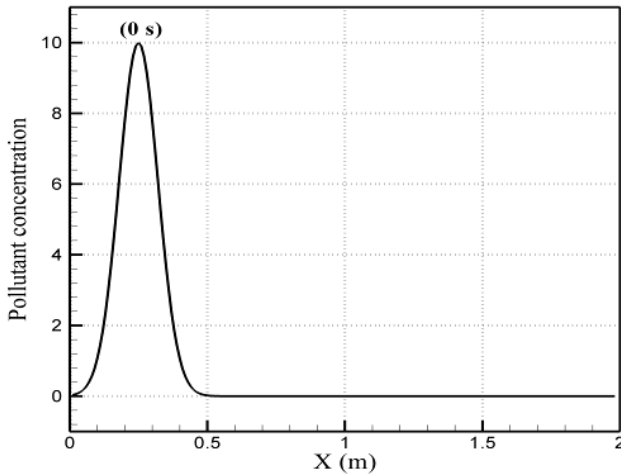


**Figure 10.** Validation Test 3: Initial pollutant concentration profile along flat-bottomed channel

where  $C_1 = 10$  and  $a = 0.01$ . As time progresses, the pollutant concentration propagates as a wave of constant profile that moves along the channel to the right at constant speed  $u = 0.5\text{ m/s}$ . In the numerical tests, we consider the propagation of this wave over several different meshes and using the Van Albada and Minmod limiters. The simulation results are

grouped under three scenarios depending on the type of mesh used (see Figure 11):

I- Coarse fixed mesh (279 elements, 180 nodes) without adaptation (Figure 11a).

II- Coarse mesh with adaptation (Figure 11b).

III- Fine fixed mesh (2174 elements, 1198 nodes) without adaptation (Figure 11c).

Open boundary conditions are applied at the inlet and outlet of the channel. The lateral walls are slip. The CFL value used here is 0.9.

Figures 12, 13, and 14 present comparisons of the numerical predictions with the analytical solution of the evolving concentration profile along the channel for the different limiters on a coarse fixed mesh, an adapted initially coarse mesh, and a refined fixed mesh. From Figure 12, it can be seen that the numerical prediction obtained using the Van Albada limiter is significantly less diffusive (and hence more accurate) than that using the Minmod one. The diffusive effect increases progressively with simulation time, with the amplitude of the initial concentration hump reducing by  $\sim 27\%$  for the Van Albada limiter and  $\sim 60\%$  for the Minmod limiter at time  $t = 25\text{ s}$ . Small non-physical oscillations can be discerned immediately in front and behind the evolved concentration hump obtained using the Van Albada limiter on the coarse fixed mesh (see the close-up inset of Figure 12). These drawbacks are much less evident in the results obtained on the fine fixed mesh using the Van Albada limiter. Figure 14 shows that the amplitude of the concentration profile computed on the fine fixed mesh is better maintained and non-physical oscillations are almost eliminated. However, the CPU time (Table 2) required on the fine fixed mesh is 12 times longer than on the fixed coarse mesh for the Van Albada limiter. Figure 13 shows the results obtained on an adaptive mesh, commencing from a coarse mesh and refining according to formula (25). In this case, the numerical predictions obtained by the Roe scheme coupled with the Van Albada limiter are much improved over those on the fixed coarse mesh, with the concentration wave amplitude remaining within 5% of the analytical solution. Numerical dissipation is greatly reduced, and the CPU simulation time is more than 2 times faster than on the fine fixed mesh (Table 2).

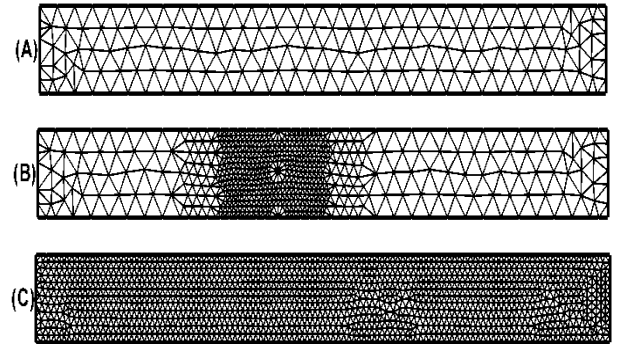


**Figure 11.** Validation Test 3: Meshes: (a) coarse, (b) adaptive at  $t = 12.27\text{ s}$  and (c) refined

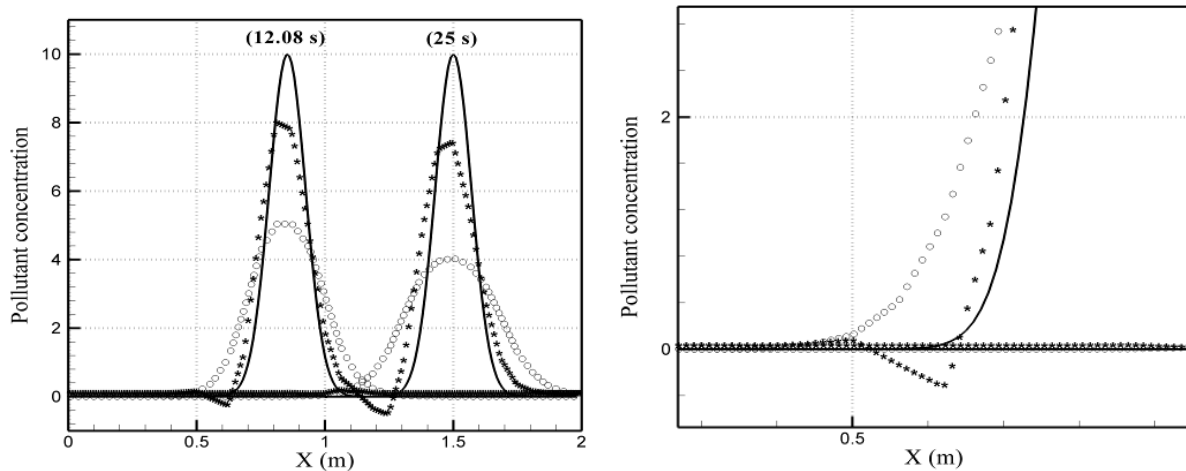


**Figure 12.** Validation Test 3: (a) pollutant concentration profile obtained using different limiters on the coarse mesh, (b) close-up view of profile near  $x = 0.5$  m. (stars = Van Albada limiter, circles = Minmod limiter, solid line = exact solution.)

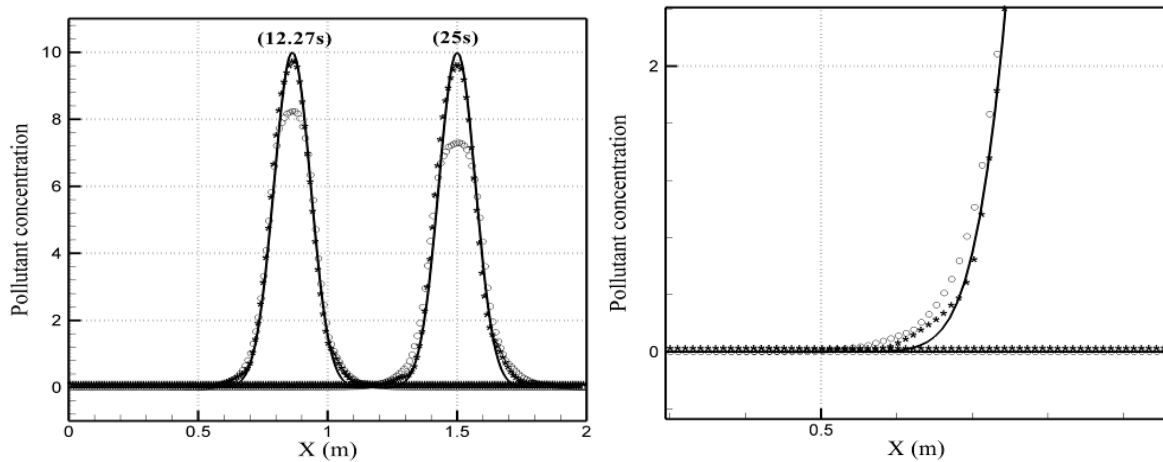


**Figure 13.** Validation Test 3: (a) pollutant concentration profile obtained using different limiters on the adapted coarse mesh, (b) close-up view of profile near  $x = 0.5$  m. (stars = Van Albada limiter, circles = Minmod limiter, solid line = exact solution.)

**Table 2.** Validation Test 3: pollutant advection in a flat-bottomed channel: performance of Roe scheme for different meshes

Coarse meshes without adaptation

		# elements	# points	C(max)	C(min)	CPU time (s)
Exact		--	--	10	0	--
12.08s	Minmod	279	180	5.083	0.000	41.3
	Van Albada			7.893	-0.341	28.90
25s	Minmod			4.038	0.000	86.92
	Van Albada			7.298	-0.599	60.06

Coarse meshes with adaptation

		# elements	# points	C(max)	C(min)	CPU time (s)
Exact		--	--	10	0	--
12.27s	Minmod	1095	608	8.238	0.000	354.75
	Van Albada	1035	577	9.621	-0.013	228.23
25s	Minmod	1063	593	7.295	0.000	720.54
	Van Albada	1053	586	9.505	-0.011	450.01
	Van Albada	2174	1198	9.6469	-0.058	730.50

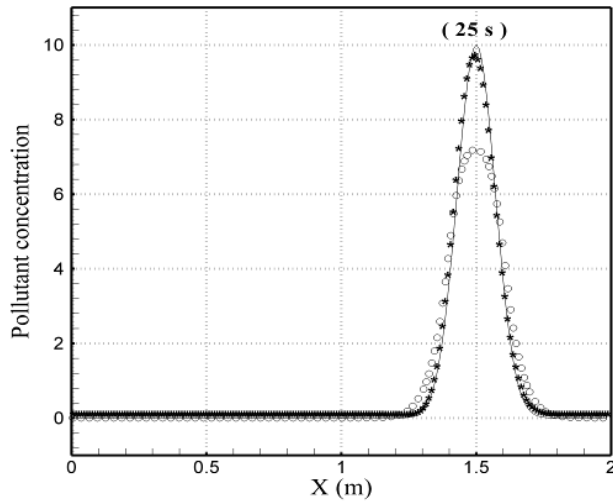


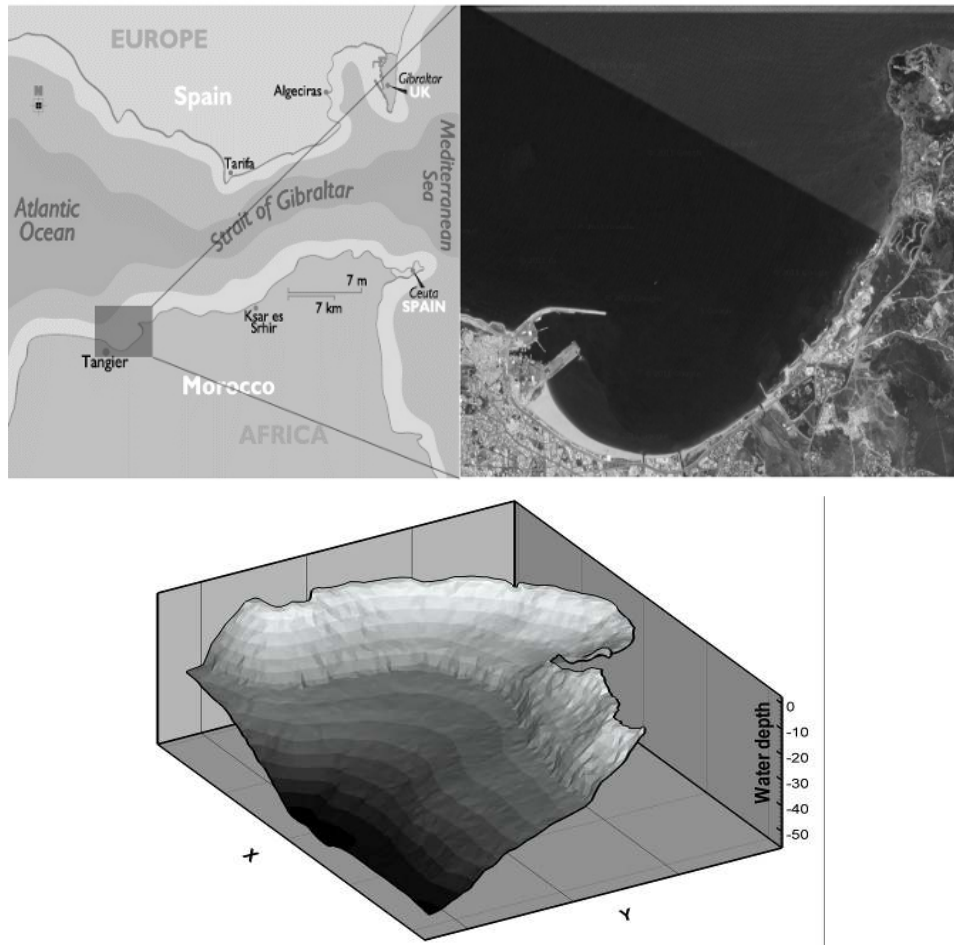
**Figure 14.** Validation Test 3: pollutant concentration profile obtained using different limiters on the fine fixed mesh. (stars = Van Albada limiter, circles = Minmod limiter, solid line = exact solution.)

## 6. Simulation of Pollutant Plume in the Bay of Tangier

The Bay of Tangier (Figure 15) is a semi-enclosed shallow basin located on the west coast of the southern Strait of

Gibraltar. The Moroccan city of Tangier is located immediately inland of the shore of the bay. The bed topography is spatially quite non-uniform, with the mean water depth increasing progressively from 0 m at the shore to about 50 m at the interface with the greater Mediterranean Sea. The vertical flow structure in the Bay of Tangier consists of an upper layer of incoming cold fresh surface Atlantic water overlying a deep current of outgoing warmer salt water[22, 23]. The bay is heavily used by shipping, whose volume has grown since the recent development of a Mediterranean port at Tangier. Assessment of the environmental risk is therefore required, and the present numerical tool is being developed with this longer-term aim in mind.

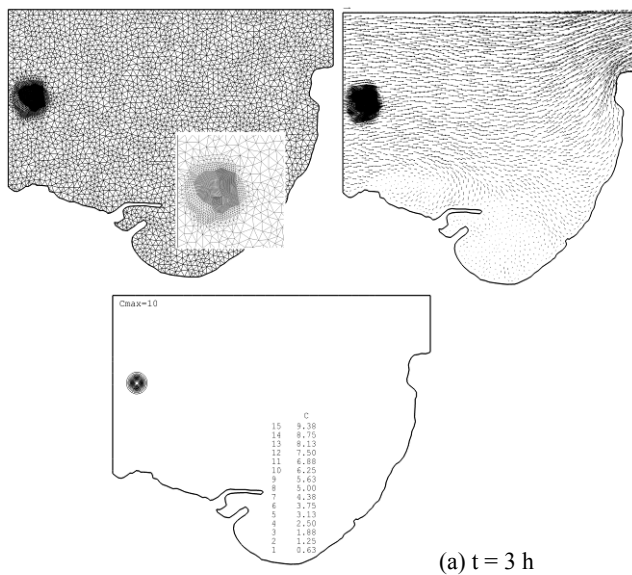
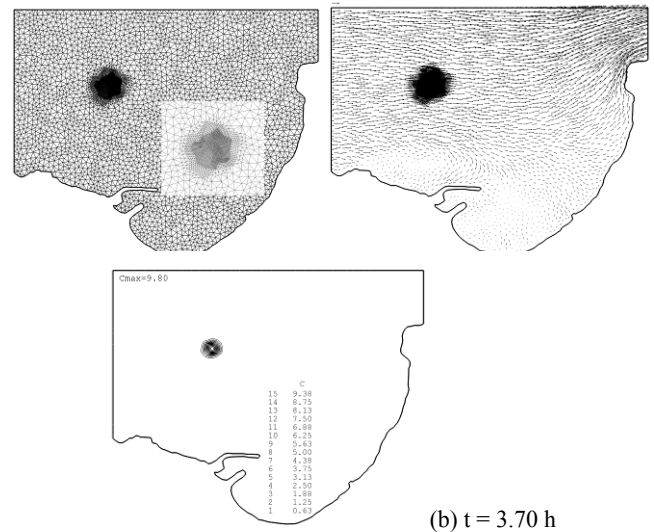
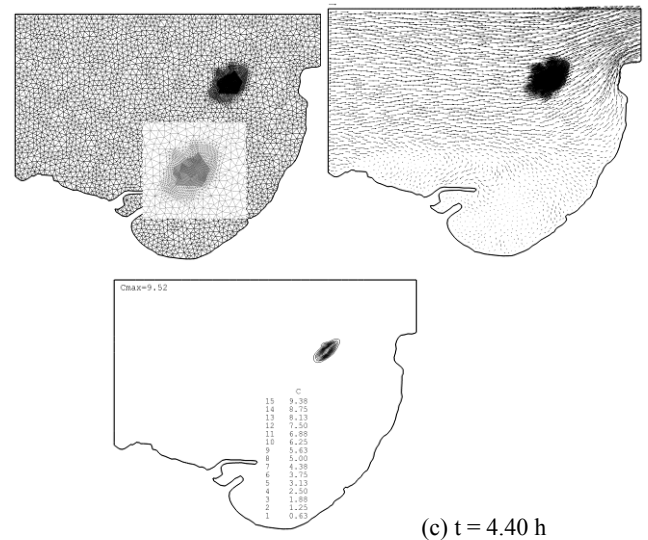
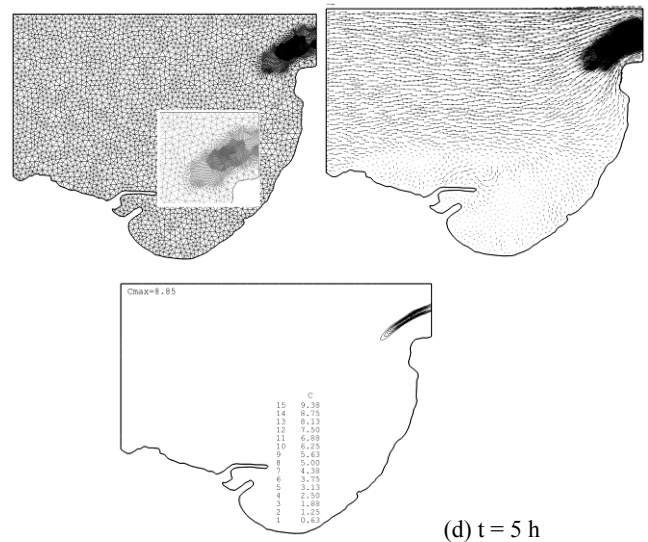
The simulations presented herein test the dynamically adaptive scheme for an idealised version of the Bay of Tangier, noting its complicated geometry and non-uniform bathymetry. An initial mesh of 5702 elements and 3000 nodes was created according to the boundary geometry for the Bay of Tangier shown in Figure 15. Then the hydrodynamic module was used to simulate the flow field within the bay. At a prescribed time, pollutant was injected into the fully established flow field. The concentration of the injected pollutant is given by



**Figure 15.** Plan and 2D views of the Bay of Tangier study area and its bathymetry

$$C_0 = C_1 \exp \left[ -\frac{(x-x_1)^2 + (y-y_1)^2}{r^2} \right]$$

where the initial pollutant concentration is  $C_1 = 10$ ,  $x_1 = 500$  m,  $y_1 = 4500$  m, and  $r = 150$  m. We assume a constant diffusion coefficient  $D_x = D_y = 0.001$  m<sup>2</sup>/s. coefficient is set to  $n_M = 0.001$  s/m<sup>1/3</sup>. The flow is forced by a constant velocity profile on the western boundary of the domain, which decreases linearly from 1 m/s at the northwest corner of the domain to 0 at the western shoreline. There is no wetting and drying. Figure 16 shows the results obtained using the Van Albada limiter on the adaptive mesh at times  $t = 3$  h (when the pollutant is released), 3.70 h, 4.40 h and 5 h. The Figure has three columns. The first presents the adapted mesh, the second the velocity vector field, and the third the pollutant concentration distribution. A close-up is also included of the local mesh in the vicinity of the pollutant plume. The results show the convection of the pollutant from the time of its injection, as it advects with the water currents in the bay. The mesh adapts according to the pollutant concentration gradient (25) in order to capture the frontal behaviour of the plume. The maximum pollutant concentration reduces by 5% at  $t = 3.70$  h and 20% at  $t = 5$  h. The CPU time required to simulate the results at  $t = 3, 3.70, 4.40$  and  $5$  h is respectively 0.9, 1.8, 2.7 and 3.2 h (including the hydrodynamic simulation time required to establish the flow field before injection of the pollutant). The simulation was run on the same PC Pentium (Dual Core CPU - 1.5GHz) as the previous examples. It is therefore found that the Roe-Vazquez approach coupled with the Van Albada limiter on a dynamically adaptive mesh has facilitated a PC based model of pollution in the Bay of Tangier that runs at about half real-time giving plausible results at high resolution in regions where the gradients of concentration and flow variables are locally high.

(a)  $t = 3$  h(b)  $t = 3.70$  h(c)  $t = 4.40$  h(d)  $t = 5$  h

**Figure 16.** Bay of Tangier: adapted meshes (first column), velocity vectors (second column) and pollutant concentration (third column) at different simulation times

## 7. Conclusions

This paper has described a numerical model for simulating pollutant transport in the Bay of Tangier on the south side of the Strait of Gibraltar. The numerical model solves the coupled non-linear shallow water and advection–diffusion equations by means of a second-order Godunov-type finite volume method on dynamically adaptive unstructured meshes. Attention has been given to ensuring that the flux gradient and source terms are properly balanced. Excellent agreement is achieved between the model predictions and Goutal’s[19] analytical solution for steady unidirectional flow over irregular bed topography, confirming that the scheme is correctly handling spatial bed gradients in the vector of source terms. Results in close agreement with experimental data by Denham and Patrick[27] confirm that the model simulates advective and diffusive processes that characterise separation and recirculation effects in a channel with a sidewall expansion. The third validation test of pollutant advection in a flat-bottomed channel demonstrated that use of the Van Albada limiter led to less diffusive but slightly more oscillatory results than for the Minmod limiter. For the same case, it was demonstrated that the use of a dynamically adaptive mesh led to a significant speed up in computational time over a fixed fine mesh, while retaining accuracy. The application to the Bay of Tangier, though highly idealised, indicates the potential of the model in simulating pollutant transport at field scale for a situation involving complicated coastal geometry and beach topography. The method provides a relatively quick simulation (at about half real-time on a PC) that, with better input data and after proper calibration to field measurements, could be used in practice to provide water quality predictions useful in the environmental assessment of the Bay of Tangier. Further studies should be performed in future, investigating chemical reactions and the influence of wind intensities and direction.

## Nomenclature

$\mathbf{A}(\tilde{\mathbf{W}}, \tilde{\mathbf{n}}_{ij})$	flux Jacobian evaluated using Roe’s
$\tilde{c}$	average state
$\tilde{c}$	wave celerity
$C$	pollutant concentration ( $\mu\text{g/l}$ )
$CFL$	Courant number
$\text{Crit}(\tau_i)$	adaptation criterion for cell $\tau_i$
$d_{ij}$	the sum of distances between $x_i$ and $\Gamma_{ij}$ and $y_i$ and $\Gamma_{ij}$
	$d_{ij} = d(x_i, \Gamma_{ij}) + d(x_j, \Gamma_{ij})$
$D_x, D_y$	pollutant diffusion coefficients in x- and y- directions ( $\text{m}^2/\text{s}$ )
$\mathbf{F}_1, \mathbf{F}_2$	inviscid flux component vectors
$\tilde{\mathbf{F}}_1, \tilde{\mathbf{F}}_2$	diffusive flux component vectors

$G$	acceleration due to gravity ( $\text{m/s}^2$ )
$h$	total depth from the sea bed to the free surface (m)
$L$	list of triangles for coarsening or refinement
$\mathbf{L}$	left eigenvector matrix of $A$
$L_{ij}$	edge length of $\Gamma_{ij}$
$m$	required adaptation level
$\text{meas}(\Gamma_{ij})$	edge length of $\Gamma_{ij}$
$n$	time step counter
$n_M$	Manning coefficient
$\tilde{\mathbf{n}}_{ij} = (n_x, n_y)$	unit vector normal to $\Gamma_{ij}$ , pointing towards cell $V_j$
$N(i)$	set of neighbouring triangles of cell $V_i$
$\mathbf{N}_{ij}$	distance vector between barycentre coordinates of cells $V_i$ and $V_j$ .
$\mathbf{R}$	right eigenvector matrix of $A$
$\mathbf{S}$	vector of source terms
$\tilde{\mathbf{S}}^n$	approximation to the source term on the cell interface $\Gamma_{ij}$
$S_{fx}, S_{fy}$	bed shear stress components
$t$	time (s)
$t^n$	time, $t_n = n\Delta t$ (s)
$u, v$	Cartesian components of depth-averaged velocity (m/s)
$V_i$	volume of i-th computational cell
$\mathbf{W}$	vector of dependent variables
$x, y$	Cartesian horizontal distances from origin
$Z_b$	bed elevation above a fixed horizontal datum (m)
$\Delta t$	time step
$\Gamma_{ij}$	common edge of two neighbouring cells $V_i$ and $V_j$
$\rho$	water density ( $\text{kg/m}^3$ )
$\Phi$	numerical flux vector
$ \Lambda $	diagonal matrix of the absolute values of the eigenvector of $A$
$\Psi^n$	numerical source vector
$\theta_i(\mathbf{X}, \mathbf{Y})$	quadratic functional

## REFERENCES

- [1] P. L. Roe, Approximate Riemann Solvers, Parameter Vectors and Difference Schemes, 43, 357-372, 1981.

- [2] F. Alcrudo, P. Garcia-Navarro, A high resolution Godunov-type scheme in finite volumes for the 2D shallow-water equations, *International Journal for Numerical Methods in Fluids*, 16, 489-505, 1993.
- [3] M. E. Hubbard, P. Garcia-Navarro, Flux difference splitting and the balancing of source terms and flux gradients, *Journal of Computational Physics*, 165, 89–125, 2000.
- [4] R. J. Leveque, Balancing source terms and flux gradients in high-resolution Godunov methods: the quasi-steady wave-propagation algorithm, *Journal of Computational Physics*, 146, 346-365, 1998.
- [5] M. Nujic, Efficient implementation of non-oscillatory schemes of free surface flows. *Journal of Hydraulic Resources*, 33(1), 101-111, 1995.
- [6] X. D. Liu, S. Osher, T. Chan, Weighted essentially non-oscillatory schemes, *Journal of Computational Physics*, 115 (1), 200–212, 1994.
- [7] T. Yoon, S. Kang, Finite Volume Model for Two-Dimensional Shallow Water Flows on Unstructured Grids, *Journal of Hydraulic Engineering*, 130, 678–688, 2004.
- [8] A. Bermudez, M. E. Vazquez, Upwind methods for hyperbolic conservation laws with source terms. *Computers & Fluids*, 23:1049–1071, 1994.
- [9] M. E. Vazquez-Cendon, Improved treatment of source terms in upwind schemes for shallow water equations in channels with irregular geometry. *Journal of Computational Physics*, 148, 497– 526, 1999.
- [10] F. Alcrudo, P. Garcia-Navarro, J. M. Saviron, Flux difference splitting for 1D open channel flow equations. *International Journal for Numerical Methods in Fluids*, 14, 1009-1018, 1992.
- [11] L. A. Monthe, F. Benkhaldoun, I. Elmahi, Positivity preserving finite volume Roe schemes for transport diffusion equations, *Computer Methods in Applied Mechanics and Engineerings*, 178, 215-232, 1999.
- [12] A. Bermudez, M. E. Vazquez-Cendon, Upwind methods for hyperbolic conservation laws with source terms, *Computers & Fluids*, 23,1049–1071, 1994.
- [13] A. Bermudez, A. Dervieux, J.A. Desideri, M. E. Vazquez, Upwind schemes for the tow-dimensional shallow water equations with variable depth using unstructured meshes, *Computer Methods in Applied Mechanics Engineerings*, 155, 49-72, 1998.
- [14] Ch. Hirsh, *Numerical Computation of internal and external flows: the fundamentals of computational fluid dynamics*, volume 1, Wiley & Sons, Second Edition, 2007.
- [15] F. Benkhaldoun, I. Elmahi, M. Seaid, Well-balanced finite volume schemes for pollutant transport by shallow water equations on unstructured meshes, *Journal of Computational Physics*, 226, 80–203, 2007.
- [16] I. Elmahi, F. Benkhaldoun, R. Borghi, S. Raghay, Ignition of fuel issuing from a porous cylinder located adjacent to a heated wall: a numerical study, *Combustion Theory and Modeling*, 8, 789–809, 2004.
- [17] I. Elmahi, Schémas volumes finis pour la simulation numérique de problèmes à fronts raides en maillages non structurés adaptatifs, Ph.D, thesis, Rouen, 1999.
- [18] E.M. Chaabelasri, Contribution à la modélisation des écoulements en eaux peu profondes, avec transport de polluant (Application à la baie de Tanger), Ph.D, thesis, Univ. Mohammed I, Oujda, 2011.
- [19] N. Goutal, F. Maurel, Proceedings of the 2nd workshop on dam-break wave simulation, Laboratoire national d'hydraulique, Groupe Hydraulique Fluviale Electricité de France, France, 1997.
- [20] Aurélie Le Dissez, Damien Sous, Stéphane Vincent, Jean-Paul Caltagiron and Aldo Sottolichio, A novel implicit method for coastal hydrodynamics modeling: application to the Arcachon lagoon, *Comptes Rendus Mécanique* 333, 796-803, 2005.
- [21] Ming-Hseng Tseng, Improved treatment of source terms in TVD scheme for shallow water equations, *Advances in Water Resources*, 27, 617-629, 2004.
- [22] J.G. Lafuente, J.L. Almazan, F. Catillejo, A. Khribeche, A. Hakimi, Sea level in the Strait of Gibraltar: Tides, *Int. Hydrogr. Rev. LXVII*. 1, 111–130, 1990.
- [23] M. Gonzalez, A. Sanchez-Arcilla, Un Modelo Numérico en Elementos Finitos para la Corriente Inducida por la Marea. Aplicaciones al Estrecho de Gibraltar, *Revista Internacional de Métodos Numéricos para Calculo y Diseño en Ingenieria*. 11, 383–400, 1995.
- [24] J.G. Zhou, D.M. Causon, C.G. Mingham, D.M. Ingram, The surface gradient method for the treatment of source terms in the shallow water equations, *Journal of Computational Physics*, 20, 1–25, 2001.
- [25] F. Marche, Theoretical and numerical study of shallow water models. applications to nearshore hydrodynamics. Ph.D, thesis, Bordeaux, 2005.
- [26] J. M. Hervouet, *Hydrodynamique des écoulements à surface libre : Modélisation numérique avec la méthode des éléments finis*, Presses de l'Ecole Nationale des Ponts et Chaussées, 2003.
- [27] M. K. Denham and M.A. Patrick, Laminar flow over a downstream-facing step in a two-dimensional flow channel. *Trans. Inst. Chemical Engineers*, 52, 361-367, 1974.
- [28] F. Hermeline, Une méthode automatique de maillage en dimension n, PhD Thesis, Université de Paris 6, 1980.